Available online at www.sciencedirect.com
SCIENCE DIRECT®
Journal of the European Ceramic Society 25 (2005) 1159–1166
www.elsevier.com/locate/jeurceramsoc

An application of scanning thermal microscopy: Analysis of the thermal properties of plasma-sprayed yttria-stabilized zirconia thermal barrier coating

F. A. Guo [a], N. Trannoy [a,*], D. Gerday [b]

[a] *Unité de Thermique et d'Analyse Physique, Laboratoire d'Energétique et d'Optique, Université de Reims, BP 1039, 51687 Reims, Cedex 2, France*
[b] *CRITT-MDTS, 3 Bd. Jean Delautre, 08000 Charleville Mézières, France*

Received 8 October 2003; received in revised form 14 April 2004; accepted 20 April 2004
Available online 10 July 2004

Abstract

Yttria-stabilized zirconia coatings were deposited on Ti–6Al–4V substrate by plasma spraying. The thermal properties of the as-sprayed coating were characterized using a scanning thermal microscopy that allows thermal conductivity to be mapped down to the submicrometer scale. The analysis of the thermal properties shows the variations in thermal conductivity with the characteristics of the materials. The relation between microstructural features and thermal conductivity was discussed in correlation with the heat conduction mechanism in different layers. Based on the experiments, the thermal probe was calibrated and the thermal conductivities of the coating and the substrate were estimated. Experimental results and thermal conductivity estimation demonstrate that the SThM analyses can be used as a powerful tool for the thermal property and microstructure analysis of plasma-sprayed thermal barrier coating.

Keywords: ZrO_2; YSZ; Plasma spraying; Ti–6Al–4V alloy; Scanning thermal microscopy; Thermal barrier coatings

1. Introduction

Although Ti–6Al–4V is one of the most widely used titanium alloys in aerospace engineering due to its unique high strength–weight ratio,[1] it shows a lack of mechanical and thermal properties at high temperature. Therefore, protective coatings are frequently required to insulate the alloy surfaces for the successful application and performance of this alloy in aerospace gas turbines.

Thermal barrier coatings (TBCs) have played an increasingly important role in enhancing gas turbine engine durability and performance.[2] For example, a TBC on Ti–6Al–4V alloy, in which the ceramic side contacting with high temperature offers heat resistance, and the metallic side contacting with low temperature provides mechanical strength and thermal conductivity. The TBC material almost universally used is yttria-stabilized zirconia (Y_2O_3-stabilized ZrO_2). This ceramic has performed admirably as a TBC because of its favourable combination of properties, including low thermal conductivity, phase stability to 1400 °C, and good erosion resistance, etc.[2,3]

Studies on thermophysical properties are of significance not only for fundamental research but also for applications of materials. It is known that the heat transport properties of polycrystalline materials are strongly affected by their characteristics and microstructural features.[4,5] In general, TBC materials and substrate are different materials, different chemical compositions and microstructural features determine their thermal properties at high temperature.

Scanning probe microscopes (SPMs) provide one of the few methods of imaging structures, observing phenomena, and manipulating objects with nanometer scale spatial resolution,[6] and the invention of the scanning thermal microscopy (SThM) provides a tool with which the thermal properties of materials can be evaluated on a very small scale. The SThM is based on an atomic force microscope (AFM), but uses a specialized thermal probe instead of con-

* Corresponding author. Tel.: +33 3 26 91 33 92; fax: +33 3 26 91 32 50.
E-mail address: nathalie.trannoy@univ-reims.fr (N. Trannoy).

0955-2219/$ – see front matter © 2004 Elsevier Ltd. All rights reserved.
doi:10.1016/j.jeurceramsoc.2004.04.026

ventional SiN_x tip of AFM. The SThM is developed to give simultaneously surface topography image and thermal property image of materials with micrometer or sub-micrometer spatial resolution. In SThM, the interaction between probe tip and sample is based on the heat flux.[7] Therefore, differences in temperature or thermal conductivity constitute the imaging contrast. The SThM has many potential applications, one of them is to study local variations in surface thermal properties.

Some earlier works have studied the thermal properties of Y_2O_3-stabilized ZrO_2 coatings,[8–12] most of them dealt with the influence of temperatures, coating compositions, defect distribution, grain size, or plasma-spraying process variables on the thermal properties of coatings. Many interesting results have been obtained from these studies. However, no work dealt with the analysis of the thermal properties of TBC materials by means of SThM techniques. To assist in this effort, we attempt to use SThM to characterize the thermal properties of plasma-sprayed Y_2O_3-stabilized ZrO_2 coatings on Ti–6Al–4V substrate.

In this report, Y_2O_3-stabilized ZrO_2 coatings on Ti–6Al–4V alloy were performed by plasma-spraying method. A SThM was used to map the thermal conductivity images, the thermal probe was then calibrated and the thermal conductivities of the coating and the substrate were estimated. The influence of the material characteristics and microstructural features on heat conduction was discussed in correlation with the heat conduction mechanism in different materials.

2. Experimental details

2.1. Preparation of Y_2O_3-stabilized ZrO_2 coating

Ti–6Al–4V wafers of dimensions ∅: 35 mm × 10 mm were polished, degreased in benzene using ultrasonic cleaning, rinsed in deionized water, and dried. Films of ZrO_2 with 7 wt.% Y_2O_3 were deposited by plasma spraying onto two sides of the Ti–6Al–4V substrate at room temperature. A Metco 6M plasma torch (Sulzer Metco AG, Switzerland) was used to spray the Y_2O_3-stabilized ZrO_2 coating. The final coatings with thickness of 70 μm on one side and 90 μm on the other side were sprayed. Table 1 summarizes the parameters for plasma spraying.

Table 1
Plasma spraying parameters for the investigated zirconia coatings

Powder composition	ZrO_2 + 7 wt.% Y_2O_3
Particle size (nm)	80–140
Power input (kW)	41
Prim./sec. gas (slpm)	45 Ar/15 H_2
Carrier gas flow (slpm)	3.5 Ar
Powder feed rate (g/min)	20
Stand-off distance (mm)	120

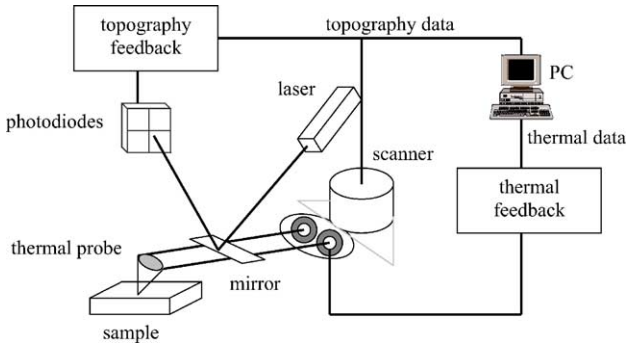

Fig. 1. Schematic diagram of the SThM set-up.

Microstructural examination was performed using a JSM 5800 scanning electronic microscopy (SEM) both on the cross-section and on the coating surface after plasma spraying and polishing according to a standard sample preparation routine.

2.2. SThM analysis

For the thermal conductivity analysis, a TopoMetrix SThM was used in which thermal imaging is achieved using a resistive thermal element incorporated at the end of a cantilever that makes it possible to achieve an AFM type feedback. The thermal element consists of a bent filament (5 μm diameter) of platinum/10% rhodium. Fig. 1 depicts the set-up of the SThM used in this work.

In SThM, normally two working modes are available: 'temperature contrast mode' and 'thermal conductivity contrast mode'. In the present work, the 'thermal conductivity contrast mode' was used, in which the thermal probe functions as a resistive heater. The control circuit uses a feedback loop to adjust the voltage applied to the bridge in order to keep the thermal probe at a constant temperature. When the probe is brought in contact with the test specimen, the probe tip cools due to heat conduction from the probe tip into the specimen. This cooling will reduce the resistivity of the probe. The current through the probe will then be increased by the bridge feedback circuit, until the temperature of the probe, and hence its resistance, is again equal to the target operating value. The amount of power required to maintain the probe at a constant temperature is directly related to the thermal conductivity of the test specimen.

The specimens used for thermal conductivity analysis were cut from the plasma-sprayed sample. The specimens were embedded in a resin so that the scanning could be carried out at the edge of the specimen. The specimens were cautiously polished in order to avoid the surface influence on the heat conduction. The SThM scanning was carried out on the cross-section of the sample that includes the coating layer and the substrate. A series of scanning of different dimensions were carried out, conducted at a temperature of 116.9 °C in order to avoid the influence of water on heat conduction on the sample surface.[13] The scan rate is 10 μm/s,

and a resolution of 400 lines per scan. The spatial resolution of the probe used in this work is about 1 μm. The error of the calculation, which is estimated by the deviation of the measured V_{air} and V_{total}, is about 5%.

3. Results and discussion

3.1. Microstructure analysis

Fig. 2 presents a typical SEM microstructure of the as-sprayed Y_2O_3-stabilized ZrO_2 coating in the cross section, with several features indicated by the arrows. The coating is porous, with microcracks, interlamellae gaps, and cavities which could be the result of pull-out during the metallographic sample preparation. Fig. 3 shows a SEM microstructure of the coating surface. Some partially melted particles, microcracks and pores can be observed in the coating. These features can play an important role in the thermal conduction in the coating.

3.2. Thermal conductivity variation

Scanning thermal microscopy provides information on thermal conductivity maps not available to conventional AFM and scanning tunneling microscopy (STM). This offers valuable opportunity to characterize the thermal properties of material surfaces at the submicrometer scale.

Fig. 4a and b show a thermal image and topographical image of a cross-sectional scanning in the thermal conductivity contrast mode. The upper parts of the images correspond to the substrate of the sample, and the lower parts are the Y_2O_3-stabilized ZrO_2 coating. It can be observed that

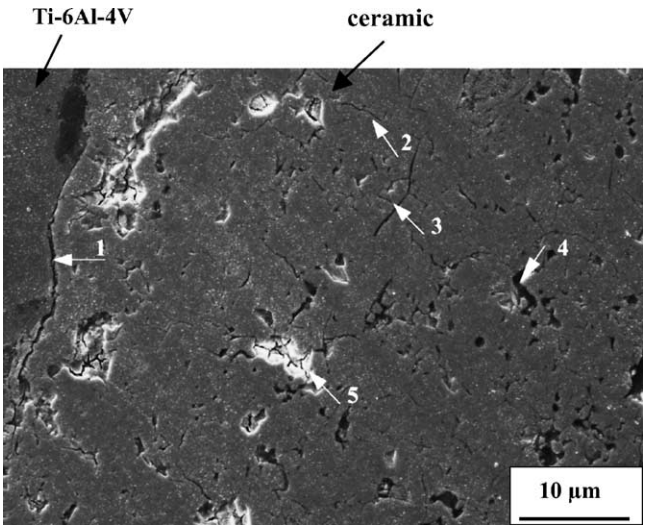

Fig. 2. SEM micrograph of polished cross section. Arrow 1 indicates a crack between the coating and the substrate; arrow 2, a vertical microcrack; arrow 3, an interlamellae gap; arrow 4, a pore; and arrow 5, a cavity which could be the result of pull-out during the metallographic sample preparation.

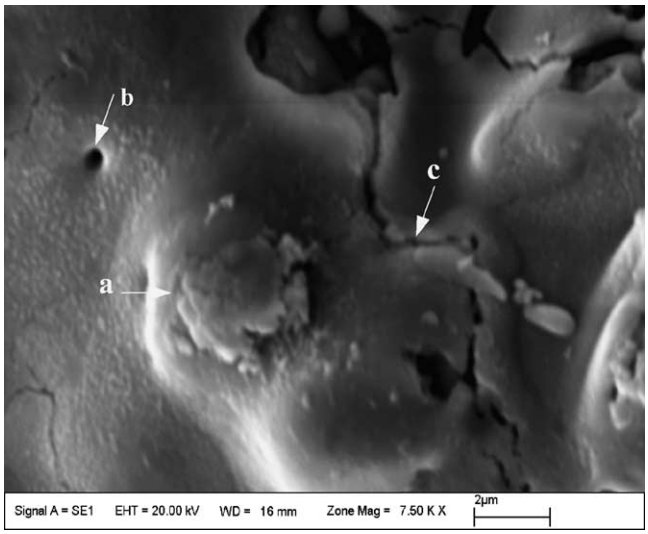

Fig. 3. SEM micrograph of the coating surface: (a) partially melted particles, (b) pore, and (c) microcrack.

the coating and substrate are interlinked and their interface is rough and uneven. At some locations, coating particles penetrate the substrate and form a tight combination. This means that the coherence mechanism of coating and substrate is mainly by mechanical combination. This observation is in good agreement with the results obtained by SEM experiments.

In SThM experiments, It should be pointed out that the resolution of the topographical images, which is related to the loop shape of the probe tip wire, is much lower than that of AFM topographical images. Despite this, the topographical image analysis easily revealed large pores and other defects such as cracks at the ceramic/substrate interface, as indicated by the arrows in Fig. 4b.

In SThM, the thermal image signal is affected by several factors, including sample thermal conductivity, probe-sample temperature differential, and probe-sample effective contact area, etc. In Fig. 4a, spots 1 and 3 were induced by the pores in the coating. In these regions, the probe-sample effective contact areas increase, the heat flows from the probe tip to the sample increase, brighter spots appear in the thermal conductivity image. In contrast, spots 2 and 4 could be induced by the dusts on the sample surface, their thermal conductivity is lower, dimmer spots appear in the thermal conductivity image. The corresponding features in the topographical image, however, show opposite contrast, as can be seen in the topographical image indicated by the same numbers.

Although thermal conductivity images to some extent depend on surface topography, thermal conductivity differences still dominate their contrast. Comparing the topographical image and thermal conductivity image in Fig. 4, it can be observed that, although many defects exist in the coating, and the coating surface is rough (see the topographical value in Fig. 4b), except some large defects, a relatively

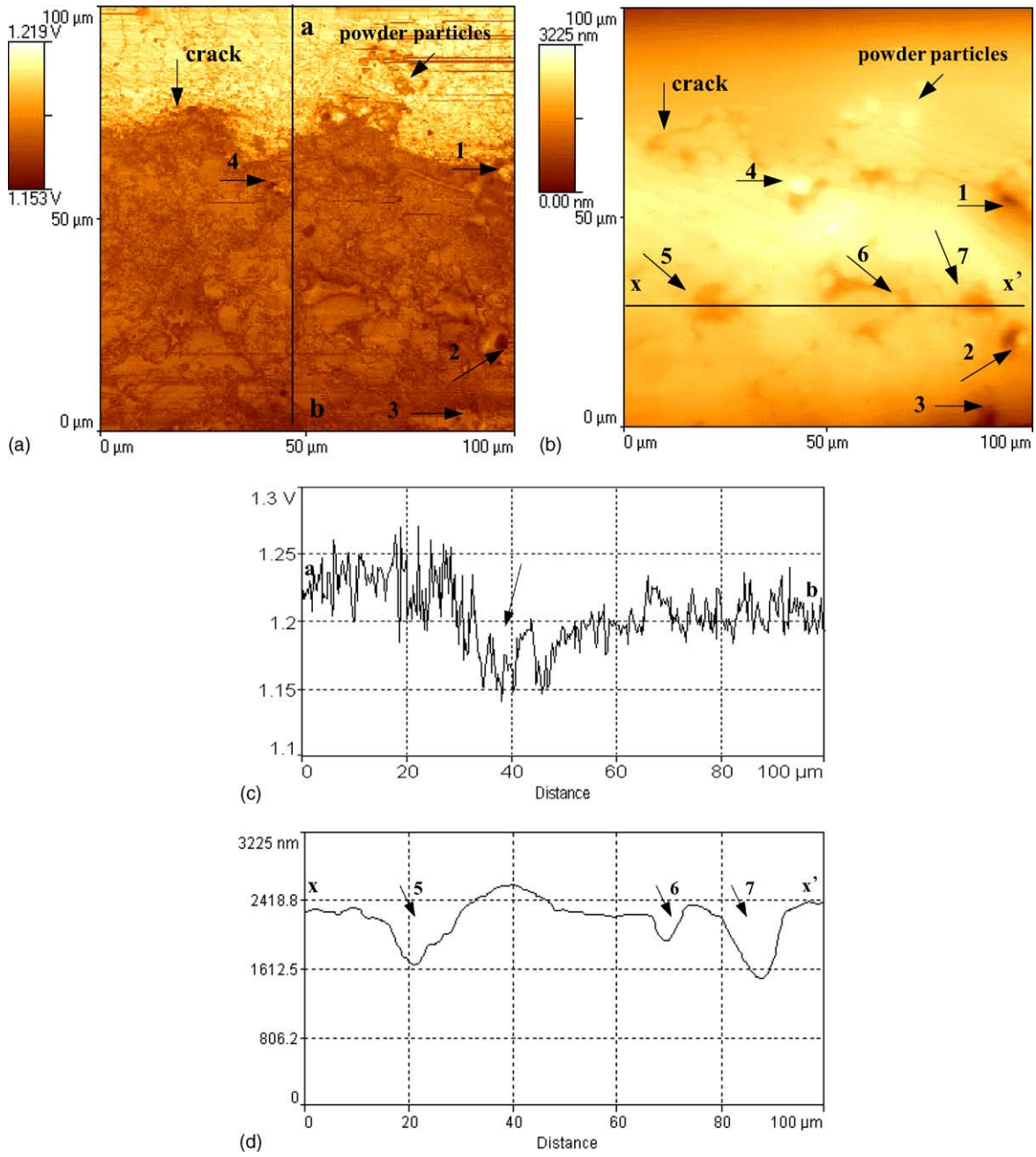

Fig. 4. (a) Thermal conductivity image, (b) topographical image, (c) thermal conductivity distribution across ab indicated in (a), and (d) defect distribution across *xx*′ indicated in (b).

uniform contrast was obtained. In the present study, for the thermal conductivity estimation, we used the average voltage values for each estimated region, and tried to avoid the influence of the defects on the thermal values, the influence of the contrast on the average thermal values can be neglected.

Fig. 4c shows the thermal conductivity distribution across ab indicated in Fig. 4a. It can be observed that the thermal conductivity of the coating decreases substantially as compared with that of the substrate. This clearly shows the thermal conductivity dependence on the characteristics of the material. It can also be seen that, between the substrate and the coating, there exists a region (indicated by an arrow) where the thermal conductivity is obviously lower than that of the substrate and the rest of the coating. This is mainly due to the higher defect density in this region, as can be seen in the topographical image and in Fig. 2.

In the spraying process, the melted powder particles impact on the substrate surface at high speed, then flow and deform along the substrate surface, finally forming a bonding microstructure in the coating. Because the coating consists of melted and half-melted particles heaped up the layer, and since the thermal expansion characteristics of the substrate and ceramic are obviously different, many pores and microcracks formed in the coating, especially close to the sub-

strate/coating interface, the defect density is much higher. Therefore, the imperfections in the coating are mainly due to the inherent nature of the plasma-spraying process and might be present in each plasma-sprayed coating.

The thermal conductivity image was obtained by recording the Wheatstone bridge voltage (see Fig. 1b). It will require more heat flows from the thermal probe to the locations having higher thermal conductivity than to the places with lower thermal conductivity. It is well known that, in electrically insulating materials, the dominant mode of heat transfer is mainly through phonon motion;[14] in contrast, the thermal conduction in metals includes electron conduction and phonon conduction.[15] Therefore, the characteristics of the materials determine that the substrate has a higher thermal conductivity than that of the Y_2O_3-stabilized ZrO_2 coating. As a result, more heat flow from the thermal probe to the substrate than to the coating. In order to keep the thermal probe at a constant temperature, the probe requires a higher power compensation over the substrate which, therefore, appear brighter in the thermal conductivity image, as can be seen in Fig. 4a.

On the other hand, the defects within the coating have a significant influence on the thermal conduction. Pores, filled with gas of a lower thermal conductivity than the solid phase, help block the heat flow and thus make the material more insulating. Interfaces and grain boundaries, which are crossed by the heat flow path, can also inhibit heat conduction. The impurities and the second phase Y_2O_3 located at the grain boundaries reduce the effective across sectional area of the sample, thereby lower the thermal conductivity. Therefore, the cross-sectional thermal conductivity profile can also provide information on the imperfection distribution in the coating layer.

Fig. 4d shows the defect distribution across xx' indicated in Fig. 4b. Using the image analysis process, the dimensions of these defects can be evaluated: the dimensions of the defect 5, 6 and 7 are about ∅: 12.5 μm × 0.6 μm, ∅: 5.2 μm × 0.3 μm and ∅: 11.8 μm × 0.9 μm, respectively.

3.3. Estimation of the thickness of the coating layer

In the SThM thermal image regions showing different thermal conductivities, and hence the thermal conductivity contrast variation can be observed which is mainly due to the different characteristics and microstructural features of the coating and substrate. Therefore, the SThM analyses can also be used to estimate the thickness of the coating at different scanning locations.

Fig. 5a and b exhibit a thermal conductivity image and variations in thermal conductivity across ae indicated in Fig. 5a. It can be observed that, from a to b, the thermal conductivity distribution is approximately stable, then from b to c, the thermal conductivity is obviously lower than that of a and b and c and d, which is mainly due to the higher defect density in this region, as discussed above. From c to d, the thermal conductivity becomes stable, and from d to e, it decreases and becomes stable again. Since the scanning was conducted at the edge of the sample, and the sample was embedded in the resin, it is reasonable to deduce that, from a to b, it is in the substrate region, from b to d, is the Y_2O_3-stabilized ZrO_2 coating layer, then, from d to e, is the resin layer, and the thickness of the coating is about 88 μm.

Fig. 6a and b show another thermal conductivity image and variations in thermal conductivity across ae indicated in Fig. 6a while scanning from the substrate to the resin on the other side of the sample. Similarly, the thickness of the coating is deduced to be about 75 μm.

The thickness of the coating at different scanning locations deduced by the thermal conductivity contrast are consistent with those obtained by optical microscopy experi-

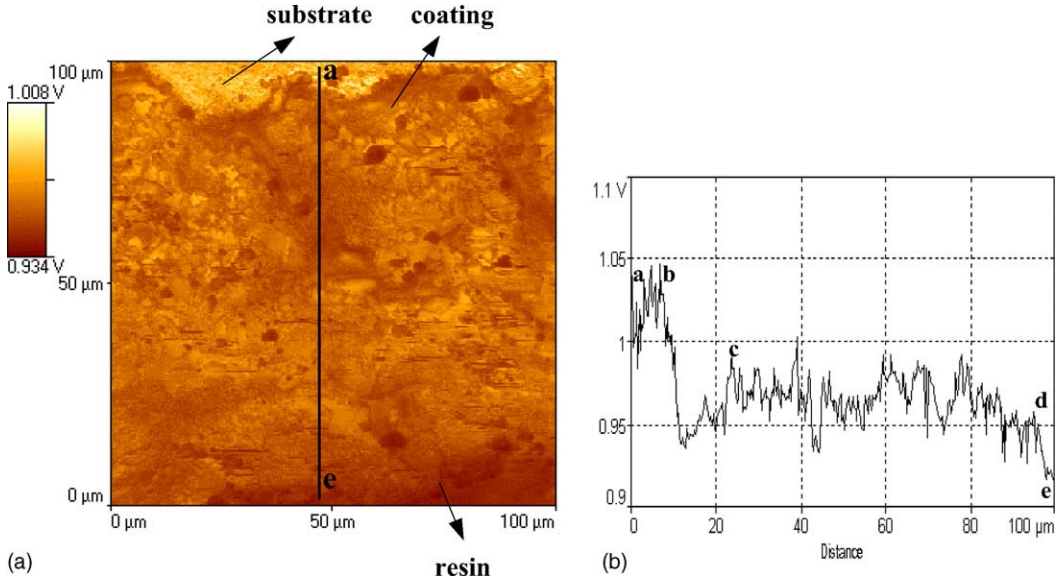

Fig. 5. (a) Thermal conductivity image and (b) thermal conductivity distribution across ae indicated in (a).

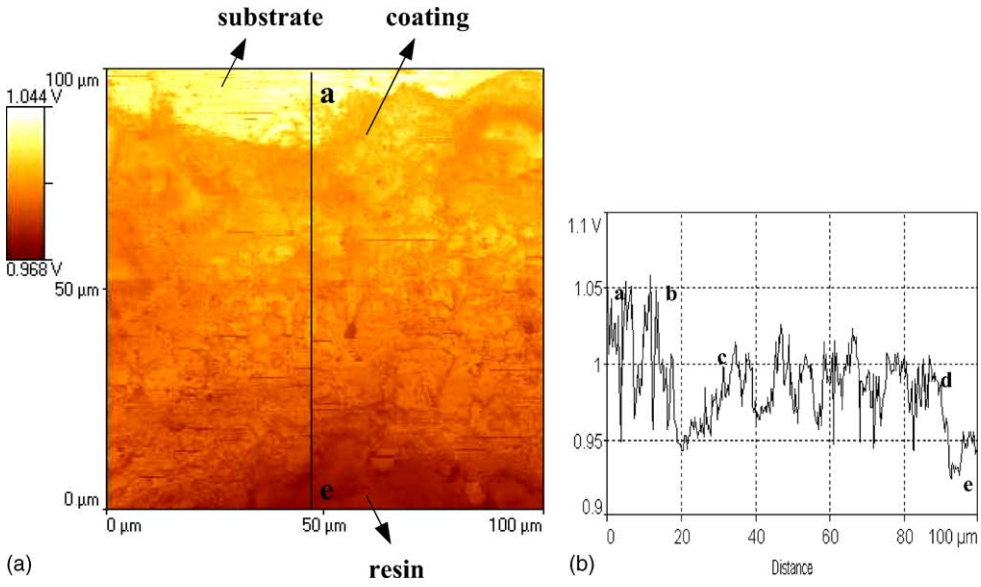

Fig. 6. (a) Thermal conductivity image and (b) thermal conductivity distribution across ae indicated in (a).

ments. These observations suggest that the SThM is a powerful tool which can easily detect the thickness of the coating with a simple sample preparation.

3.4. Thermal conductivity estimation

For the thermal conductivity estimation, we calibrated the thermal probe used in this work. When the probe tip is in the air (far away from the sample surface), the heat flow dissipated into the tip Q_{air} is given by:

$$Q_{air} = \frac{V_{air}^2}{R_{op}} \tag{1}$$

where V_{air} is the voltage across the probe tip (determined by the bridge circuit), R_{op} is the probe tip resistance at the operating temperature (T_{op}). R_{op} is determined by the following relation:[16]

$$R_{op} = R_0[1 + \alpha_p(T_{op} - T_0)] \tag{2}$$

where R_0 is the probe tip resistance at ambient temperature, α_p ($=0.00165\,\Omega(\Omega\,\mathrm{K})^{-1}$) is the resistance coefficient of the platinum/10% rhodium thermoresistive filament, T_0 is the ambient temperature.

When the probe tip is brought in contact with the sample, the total heat dissipated into the probe tip Q_{total} is given by:

$$Q_{total} = \frac{V_{total}^2}{R_{op}} \tag{3}$$

V_{total} is obtained from the thermal conductivity images. Therefore, the heat flow going into the sample can be written as:

$$Q_s = Q_{total} - Q_{air} \tag{4}$$

At an operating temperature, the variation in Q_s at different scanning locations is directly related to the thermal conductivity κ_s of the microstructure.

For a given thermal probe tip, using a series of samples whose thermal conductivities are known, a relation between Q_s and κ_s can be obtained under the same scanning conditions, and hence the thermal conductivity of the studied sample can be estimated. Fig. 7 shows the relation between Q_s and κ_s for these materials. It can be seen that two segmental lines were obtained by linear fit processing: for the materials with lower thermal conductivities (less than $57\,\mathrm{W\,m^{-1}\,K^{-1}}$), the relation between Q_s and κ_s is $Q_s = 0.6905 + 0.0304\kappa_s$; and for the materials with higher thermal conductivities, the relation is: Q_s

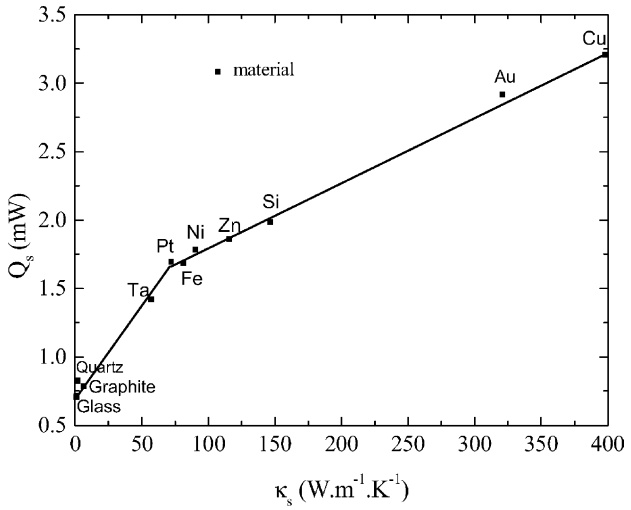

Fig. 7. Heat flow Q_s as a function of thermal conductivity κ_s for some materials with known thermal conductivities. The solid line is a least-squares fitting line.

$= 1.2170 + 0.0049\kappa_s$. This result is not in agreement with those obtained by Ruiz et al. who obtained an excellent linear relation.[17]

In order to evaluate κ_s, Q_s was calculated at each scanning location under the same scanning conditions as those for the probe calibration. As mentioned above, for the Q_s calculation, the average image voltage values were obtained from the thermal images of the estimated region. The thermal conductivities of the substrate and the coating are all less than that of pure titanium (about $20\,W\,m^{-1}\,K^{-1}$),[18] so the relation $Q_s = 0.6905 + 0.0304\kappa_s$ was used.

The thermal conductivity of the substrate estimated by this method is about $16.6\,W\,m^{-1}\,K^{-1}$, and that of the coating is about $4.2\,W\,m^{-1}\,K^{-1}$.

The thermal conductivities of the substrate and the coating obtained in this work are higher than those obtained by other method ($7.3\,W\,m^{-1}\,K^{-1}$ for the substrate, $2.5\,W\,m^{-1}\,K^{-1}$ for the coating).[19,20] This might be due to the different composition of the materials and the different experimental conditions. The results obtained in this work demonstrate that SThM is a possible method to estimate the thermal conductivities of the coating and the substrate with a simple sample preparation. However, there are some drawbacks for this method: (1) the recalibration is necessary if the probe or operating conditions are changed; (2) as discussed above, the thermal voltage values are affected by topographical factors, such as microstructure defects, atom diffusion, grain boundary features. These factors influence the thermal voltage values and thermal imaging. It is easy to understand, but difficult to separate the thermal data from the topographical data in this case. Therefore, further work should be taken in order to obtain the precise values of the thermal image signal.

4. Conclusions

In terms of SThM techniques, the Y_2O_3-stabilized ZrO_2 thermal barrier coating on Ti–6Al–4V alloy deposited by plasma-spraying was investigated. On the basis of the experiments, the following results were obtained:

1. Scanning thermal microscopy allows mapping of thermal conductivity differences of solid material surface. Therefore, the SThM analyses can be used to investigate thermophysical properties and microstructural features of materials.
2. The thickness of the plasma-sprayed coatings could be deduced by the cross-sectional thermal conductivity profile and its results are consistent with those obtained by optical microscope experiments.
3. The thermal conductivities of the coating and the substrate were estimated by calibrating the thermal probe. Although this method should be improved to make the result more reliable, it provides a possible method to determine thermal conductivities of estimated materials with a simple sample preparation.

Acknowledgements

This work is financially supported by French Ministry of Research and the Regional Council of Champagne-Ardenne France (Grant no. 2001882, CPER EN2040).

References

1. Polmear, I. J., *Light Alloys*. Edward Arnold, Landon, UK, 1989, pp. 211–271.
2. Miller, R. A., Current status of thermal barrier coatings—an overview. *Surf. Coat. Technol.* 1987, **30**, 1–11.
3. Miller, R. A., Oxidation-based model for thermal barrier coating life. *J. Am. Ceram. Soc.* 1984, **67**(8), 517–521.
4. Qian, L. H., Wang, S. C., Zhao, Y. H. and Lu, K., Microstrain effect on thermal properties of nanocrystalline Cu. *Acta Mater.* 2002, **50**, 3425–3434.
5. Yang, H. S., Bai, G. R., Thompson, L. J. and Eastman, J. A., Interfacial thermal resistance in nanocrystalline yttria-stabilized zirconia. *Acta Mater.* 2002, **50**, 2309–2317.
6. Majumdar, A., Nanoengineering: promises and challenges. *Microscale Thermophys. Eng.* 2000, **4**, 77–82.
7. Gomes, S., Trannoy, N., Grossel, P., Depasse, F., Bainier, C. and Charraut, D., D.C. scanning thermal microscopy: characterisation and interpretation of the measurement. *Int. J. Therm. Sci.* 2001, **40**, 949–958.
8. Khor, K. A. and Gu, Y. W., Thermal properties of plasma-sprayed functionally graded thermal barrier coatings. *Thin Solid Films* 2000, **372**, 104–113.
9. Chen, H., Zhou, X. M. and Ding, C. X., Investigation of the thermomechanical properties of a plasma-sprayed nanostructured zirconia coating. *J. Eur. Ceram. Soc.* 2003, **23**, 1449–1455.
10. Li, J. Q., Zeng, X. R., Tang, J. N. and Xiao, P., Fabrication and thermal properties of a YSZ–NiCr joint with an interlayer of YSZ–NiCr functionally graded material. *J. Eur. Ceram. Soc.* 2003, **23**, 1847–1853.
11. Klemens, P. G. and Gell, M., Thermal conductivity of thermal barrier coatings. *Mater. Sci. Eng.* 1998, **A245**, 143–149.
12. Schwingel, D., Taylor, R., Haubold, T., Wigren, J. and Gualco, C., Mechanical and thermophysical properties of thick PYSZ thermal barrier coating: correlation with microstructure and spraying parameters. *Surf. Coat. Technol.* 1998, **108/109**, 99–106.
13. Gomes, S., Trannoy, N. and Grossel, P., DC thermal microscopy: study of the thermal exchange between a probe and a sample. *Meas. Sci. Technol.* 1999, **10**, 805–811.
14. Kingery, W. D., The thermal conductivity of ceramic dielectrics. In *Progress in Ceramic Science, Vol 2*, ed. J. E. Burke. Pergamon Press, New York, 1962, pp. 182–235.
15. Dorlot, J. M., Baïlon, J. P. and Masounave, J., *Des matériaux, Deuxième édition revue et augmentée*. Presses internationales de l'Ecole Polytechnique de Montréal, Québec, Canada, 1999, pp. 246–266.
16. Dinwiddle, R. B., Pylkki, R. J. and West, P. E., Thermal conductivity contrast imaging with a scanning thermal microscope. In *Thermal Conductivity, Vol 22*, ed. T. W. Tong. Technomic Publishing Co., Lancaster, 1994, pp. 668–677.

17. Ruiz, F., Sun, W. D. and Pollak, F. H., Determination of the thermal conductivity of diamond-like nanocomposite films using a scanning thermal microscope. *Appl. Phys. Lett.* 1998, **13**(73), 1802–1804.
18. Goldsmith, A., Waterman, T. E. and Hirschhorn, H. J., *Handbook of Thermophysical Properties of Solid Materials, Revised ed., Vol 1: Elements*. Macmillan, New York, 1961, pp. 654–673.
19. Ezugwu, E. O. and Wang, Z. M., Titanium alloys and their machinability—a review. *J. Mater. Process. Technol.* 1997, **68**, 262–274.
20. Hasselman, D. P. H., Johnson, L. F., Bentsen, L. D., Syed, R., Lee, H. L. and Swain, M., Thermal diffusivity and conductivity of dense polycrystalline ZrO_2 ceramics: a survey. *Am. Ceram. Soc. Bull.* 1987, **66**(5), 799–806.